

DATA ARTICLE

# Numerical benchmark for damage identification in Structural Health Monitoring

Francesca Marafini<sup>1\*</sup> , Giacomo Zini<sup>1</sup>, Alberto Barontini<sup>2</sup>, Nuno Mendes<sup>3</sup>, Alice Cicirello<sup>4</sup>, Michele Betti<sup>1</sup> and Gianni Bartoli<sup>1</sup>

<sup>1</sup>Department of Civil and Environmental Engineering (DICEA), University of Florence, Florence, Italy

<sup>2</sup>Department of Engineering and Geology (InGeo), University of Chieti-Pescara, Pescara, Italy

<sup>3</sup>Department of Civil Engineering, University of Minho, Guimarães, Portugal

<sup>4</sup>Department of Engineering, University of Cambridge, Cambridge, UK

\*Corresponding author. E-mail: [francesca.marafini@unifi.it](mailto:francesca.marafini@unifi.it)

**Received:** 04 March 2026; **Revised:** -; **Accepted:** -

**Keywords:** Synthetic Data, Environmental and Operational Variability, Fast-Varying Damage, Slow-Varying Damage, Sensor Faults

## Abstract

The availability of a dataset for validation and verification purposes of novel data-driven strategies and/or hybrid physics-data approaches is currently one of the most pressing challenges in the engineering field. Data ownership, security, access and metadata handiness are currently hindering advances across many fields, particularly in Structural Health Monitoring (SHM) applications. This paper presents a simulated SHM dataset, comprised of dynamic and static measurements (i.e., acceleration and displacement), and includes the conceptual framework designed to generate it. The simulated measurements were generated to incorporate the effects of Environmental and Operational Variations (EOVs), different types of damage, measurement noise and sensor faults and malfunctions, in order to account for scenarios that may occur during real acquisitions. A fixed-fixed steel beam structure was chosen as reference for the numerical benchmark. The simulated monitoring was operated under the assumptions of a Single Degree of Freedom (SDOF) for generating acceleration records and of the Euler-Bernoulli beam for the simulated displacement measurements. The generation process involved the use of parallel computation, which is detailed within the provided open-source code. The generated data is also available open-source, thus ensuring reproducibility, repeatability and accessibility for further research. The comprehensive description of data types, formats, and collection methodologies makes this dataset a valuable resource for researchers aiming to develop or refine SHM techniques, fostering advancements in the field through accessible, high-quality synthetic data.

## Impact Statement

The proposed benchmark is designed to support the comparable evaluation of SHM methods in a fully defined, controllable environment. It enables the possibility of systematic testing through the separation of true damage sensitivity from the other simulated effects, also called confounding influences, which in real data could mimic or mask the presence of damage. In addition, it allows for the quantification of the robustness to sensor faults and malfunctions, and the repetition of ablation studies where a single effect can be included or excluded in the data simulation. Paired dynamic and static recordings also support heterogeneous data fusion and consistency checks between response types. Since the benchmark is parametrized and reproducible, it can serve as a common reference point for reporting performance and uncertainty, facilitating fairer comparison between data-driven, physics-based and hybrid approaches, and accelerating the adaptation of any damage identification methods moving from numerical to experimental and real-world testing.

## 1. Introduction

Structural Health Monitoring (SHM) methods have been increasingly applied to smart management of structures and infrastructures, with the aim of preventive cost-effective preservation of critical assets. Although many tools for monitoring, data analysis, and prediction have become available in the last decades, the validation and testing of their performance against large realistic datasets is still a challenging task due to the reduced number and limitations of the existing open access benchmarks. Real data presents intrinsic variations caused by Environmental and Operational Variabilities (EOVs), such as temperature fluctuations and changes in use. Moreover, monitoring data may be affected by additional sources of uncertainties and errors such as sensor faults or malfunctions. These factors, combined and sometimes interdependent, can hinder the interpretability of the results and mask the effects of damage in the short-term (or fast-varying damage, causing sudden drops of performance in the short-term) and in the long-term (slow-varying damage, for instance due to the natural ageing of the structure over time). To evaluate SHM techniques under controlled conditions, numerous experimental benchmarks have been developed, such as the well-known Z24 bridge [1] and Hawk T1A aircraft [2]. The time and economic constraints of damaging real prototypes needed to generate large amounts of labelled data have recently led to the adoption of numerical benchmarks. These often start from simple mechanical system formulations [3] or expand existing experimental setups [4], focusing mainly on simulations of damage scenarios. Some of these studies have integrated environmental variabilities [5] and long-term damage effects [6], but only in specific cases and never in combination with sensor faults. An account of all recent numerical benchmark studies available today in the literature is provided in Table 1<sup>1</sup>. This paper presents a synthetically generated dataset designed to provide realistic, controlled, and comprehensive SHM data, including all of the above-mentioned effects. The resulting dataset and the code written to generate it were made available in open source, for testing and benchmarking damage identification methods, addressing key open challenges in synthetic SHM data generation.

## 2. Methodology

### 2.1. Framework

The numerical generation of SHM data was designed using a straightforward and scalable approach, based on a simple but informative case study, to balance realism with computational efficiency. A generic SHM setup was considered, in which three main elements can be identified: a structural system  $H(t)$  with time-varying properties, an input excitation  $x(t)$ , and a measured response  $y(t)$  resulting from the transfer of  $x(t)$  through  $H(t)$  (see the sketch in Fig. 1). In real data, numerous influences (denoted as  $Z(t)$ ) are observed affecting each of the three components, such as changes in the system properties (e.g., temperature-dependent material variations), or in the nature of input (e.g., excitation variability), or in the acquisition conditions (e.g., sensor drift or electronic degradation) and be captured by the measured response. Such effects are commonly referred to as confounding influences as they can mask or mimic damage in the measured response. In this work, confounding influences were modelled as time-varying covariate vectors affecting the system, the input, or the measured response.<sup>2</sup>

The system was assumed to be linear but time-variant over the monitoring period. A single-input single-output configuration was considered, with one monitored Degree Of Freedom (DOF). As a reference case, a fixed-fixed steel beam subjected to varying static loads and ambient vibration excitation was selected. The beam was monitored through deflection measurements to capture its static response and acceleration signals to capture its dynamic response.

<sup>1</sup>For studies in Table 1 that are starred\*, the data are also experimental, while if the authors' names are underlined, the data or the model to generate them is available for public use.

<sup>2</sup>In this context, variability is intended to denote parameter fluctuations (like operational (OV) and environmental variability (EV)), while variation refers to the resulting changes in structural response (such as frequency shifts due to stiffness variations).

**Table 1.** Overview of selected numerical SHM benchmarks

Ref.	Year	Structure	Objective	OVs	FAST
[3]	1996	Multi Degree of Freedom (MDOF) mechanical system	Novelty detection using the transmissibility function as a feature	Harmonic excitation	1, 10 and 50% stiffness reduction
[7]*	1999	SAC Phase II Steel Moment Frame	Test control strategies after strong motion earthquakes	Ground acceleration	Stiffness reduction corresponding to an 18% reduction in frequency
[8]	2002	IASCE–ASCE SHM 2x2bay steel frame	Evaluation of SHM methods	White Gaussian Noise (WGN), Shakers	6 scenarios with braces removal or bolts loosening
[9]*	2003	IABMAS 1–2 span bridge	Test damage detection algorithms	WGN, Hammer impact, Shakers	Reduced stiffness, Boundary condition change
[10]	2017	Two offset cantilevered beams	Complex nonlinear dynamics for system identification	Load amplitude variability	No damage scenarios
[5]	2019	2-span steel beam	Validation of decision-making tools	WGN, Deterministic moving load	6 scenarios with stiffness reduction
[6]	2021	Wind turbine blade	Condition assessment of a wind turbine blade	Rotor speed changes	Cracks openings simulated as local stiffness reduction
[11]	2021	Two-story steel frame structure with Bouc–Wen hysteretic links	Validations of SHM, model reduction, and structural identification methods	Ground motion excitation scenarios	Strength and stiffness deterioration Bouc–Wen model parameter variations
[4]*	2022	Steel truss bridge (Hell Bridge Test Arena)	Hybrid SHM for DI on steel bridges	WGN	Stiffness reduction in connections

Although a beam was used here as a specific case study, the benchmark generation procedure is general and can be extended to other structural configurations and additional sources of influence. Among all possible  $Z(t)$  that could interact to shape SHM data, a selection of them was explicitly modelled, in order to reproduce real-world phenomena either directly (e.g., modelling the dependence of the Young's modulus of steel on temperature) or indirectly (e.g., simulating sensor faults a posteriori on the generated data).

The following effects were included:

- the variability of the operational static load  $p$ , including short- and long-term components;
- the variability of the ambient vibration within a fixed frequency band, with varying amplitude  $\sigma_{AV}$ ;
- the effect of the variability of the environment on material properties, modelled through an empirical relationship between steel stiffness and temperature  $T$ ;

- the effect of sudden damage (FAST), appearing as a shift in the data, modelled as a decrease in stiffness  $d_{fast}$ ;
- the effect of progressive damage (SLOW), simulating accelerated corrosion through a gradual reduction of the beam area, stiffness, and mass  $d_{slow}$ ;
- the effect of system's sensor faults and malfunctions (SF/M) applied a posteriori to the simulated data ( $sfm$ ).

The simulated effects qualitatively illustrated in Fig. 1 were simulated to act either on the input, the parameters of the structural system, or the measured output within the design setup. The dotted lines highlight cases in which confounding influences were simulated to act indirectly, for example, for environmental parameters that govern slow damage evolution or for the same evolution affecting operational conditions. The simulated monitoring covered a time span of three years, enabling the representation of both slow processes (seasonal cycles, long-term trends) and intermittent or sudden events (operational changes, fast damage, sensor faults). For static monitoring, single value hourly acquisitions of midspan deflection were generated to simulate a long-term displacement record, while for dynamic monitoring, the synthetic generated data consisted of 3-minute acceleration time histories simulating AV acquisitions. Within this framework, two models were adopted to compute the system response: a Euler-Bernoulli beam model for the static response and a linear single-degree-of-freedom (SDOF) model for the dynamic response.

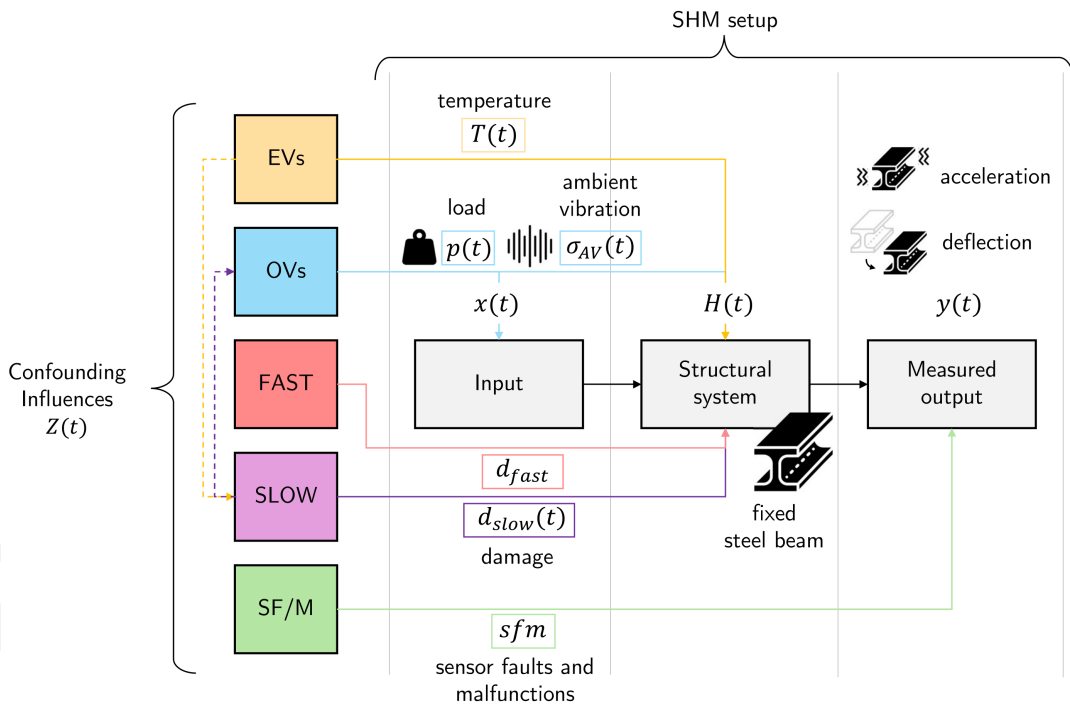


**Figure 1.** Chosen simplified SHM setup representation for the benchmark and schematic representation of the modelled confounding influences  $Z(t)$  acting on the SHM system.

In the formulations reported in Figure 2 for the simulation of the dynamic response, the SDOF stiffness considered was the beam bending stiffness  $k$  and depended on the following: the boundary conditions  $\rho$ ; the elastic modulus  $E$ , which in turn depended on the temperature varying with time  $T(t)$  and the section inertia  $I$  affected by FAST and SLOW varying damages, due to applied sudden

stiffness drops and progressive reduction of the cross-section area (damage simulations are described in Sections 3.6.3.1 and 3.6.3.2). The mass  $m$  instead was not considered affected by EVs, but only by the variability of the live load considering a slow application rate, and slightly by SLOW damage, due to the loss of volume and consequently the reduction of the cross-section. The variability in time of the ambient excitation  $\sigma_{AV}$  was applied to the input, while the SF/M were instead only applied to the measured output. The output acceleration depended on all of the above parameters. By contrast, the deflection was calculated at midspan ( $L/2$ ) according to Euler-Bernoulli, proportionally to the applied static load (OVs) and inversely to the beam bending stiffness, therefore depending on EVs (affecting the Young Modulus) and FAST and SLOW varying damage affecting  $I$  (Figure 3).

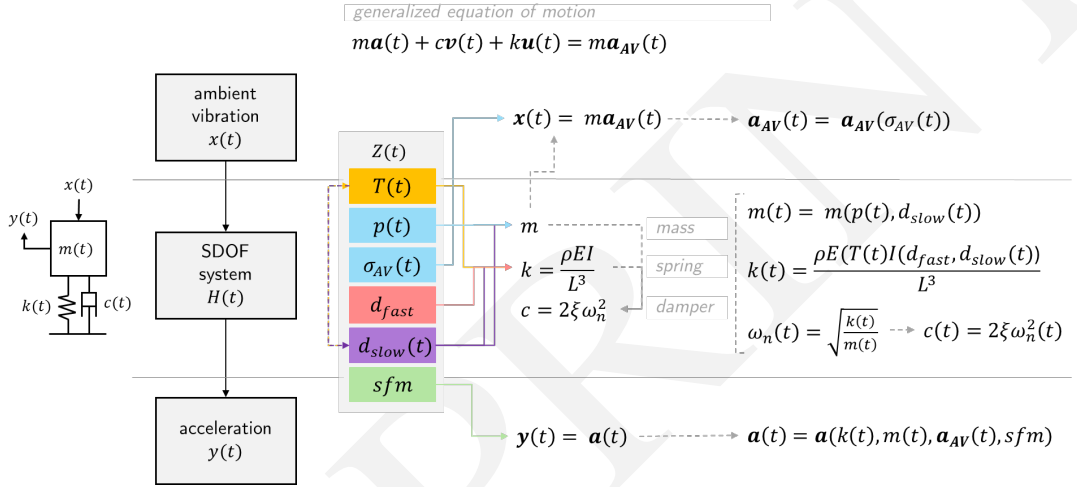


**Figure 2.** SDOF formulation including the confounding influences.

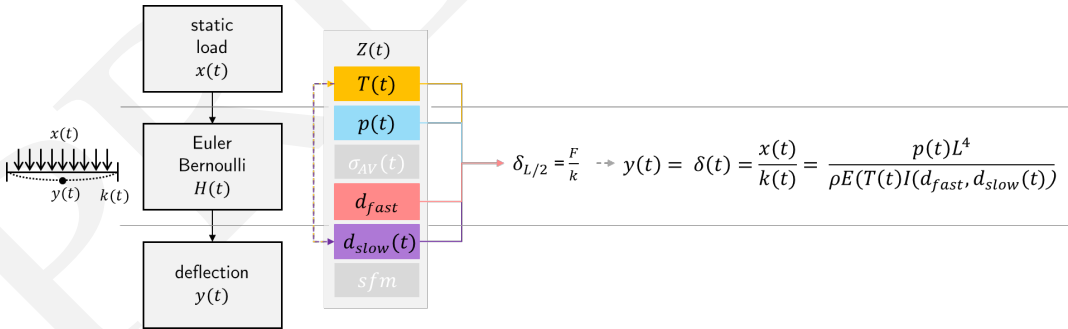


**Figure 3.** Midspan deflection calculation with Euler-Bernoulli including the confounding influences.

Moving from the time-dependent notation used in Figures 2 and 3, the cascading effect of the confounding influences was expressed by discretising the continuous-time formulations. Each acquisition was generated considering finite hourly instants at which the simulated effects, expressed as covariate parameters, were assumed constant (i.e. temperature was not considered to vary within a single 3-minute acceleration signal). Therefore, the discrete sequences of hourly acquisitions, generated over the 3-year

monitoring period, were indexed by  $i = 1, \dots, n_a$  ( $n_a$  = number of acquisitions). Each dynamic acquisition was denoted as one acceleration vector  $\mathbf{a}_i \in \mathbb{R}^{n_s}$ , where  $n_s$  is the number of samples within the acquisition. Each simulation of static measurement was denoted as the scalar  $\delta \in \mathbb{R}^1$ .

For each hourly acquisition  $i$ , the benchmark data generation was setup to simulate the cumulative effect of the variability of temperature  $T_i$ , of the operational load  $p_i$ , and two types of damage effects:  $d_{\text{FAST},i}$  for sudden events (e.g., stiffness decay indicative of rapid damage occurrence), and  $d_{\text{SLOW},i}$  for progressive damage (e.g., corrosion), and of sensor malfunction or failures denoted as  $\text{sfm}_i$ , capturing the anomalies in data not directly related to the structural health itself, applied only to the generated accelerations  $a_i$  a posteriori. The term  $\varepsilon_i$  was also included to account for potential random errors or noise within acquisition  $i$ , modelled as White Gaussian Noise (WGN). All these effects were synthetically expressed in vectors of covariates at each acquisition level as shown in Eq. 1 and Eq. 2 which show the formalisation of the qualitative models describing how each acquisition depends on its covariates. The cascading effect of the confounding influences was also expressed by discretizing the continuous-time formulations. Each acquisition was generated considering finite time hourly instants at which the simulated effects, expressed as covariate parameters, were assumed constant (i.e. temperature is not considered to vary within a single 3-minute acceleration signal). Therefore, the discrete sequences of hourly acquisitions, generated over the 3-year monitoring period, were indexed by  $i = 1, \dots, n_a$  ( $n_a$  = number of acquisitions). Each dynamic acquisition was denoted as one acceleration vector  $\mathbf{a}_i \in \mathbb{R}^{n_s}$ , where  $n_s$  is the number of samples within the acquisition. Each simulation of static measurement was denoted as the scalar  $\delta \in \mathbb{R}^1$ . In each hourly acquisition  $i$ , the benchmark data generation is setup to simulate the cumulative effect of the variability of the temperature  $T_i$ , of the operational load  $p_i$ , and two types of damage effects:  $d_{\text{fast},i}$  for sudden events (e.g., stiffness decay indicative of rapid damage occurrence), and  $d_{\text{slow},i}$  for progressive damage (e.g., corrosion), and of sensor malfunction or failures denoted as  $\text{sfm}_i$ , capturing the anomalies in data not directly related to the structural health itself, applied only to the generated accelerations  $a_i$  a posteriori. The term  $\varepsilon_i$  is also included to account for potential random errors or noise within acquisition  $i$ , modelled as White Gaussian Noise (WGN). All these effects can be expressed synthetically in vectors of covariates at each acquisition level, as shown in Eq. 1, while Eq. 2 shows the formalisation of the qualitative models describing how each acquisition depends on its covariates.

$$\begin{aligned} \mathbf{z}_i^{(\text{dyn})} &= [T_i, p_i, \sigma_{\text{AV},i}, d_{\text{fast},i}, d_{\text{slow},i}, \text{sfm}_i], \\ \mathbf{z}_i^{(\text{stat})} &= [T_i, p_i, d_{\text{fast},i}, d_{\text{slow},i}]. \end{aligned} \quad (1)$$

$$\begin{aligned} a_i &= f\left(\mathbf{z}_i^{(\text{dyn})}\right) + \varepsilon_i, \\ \delta_i &= f\left(\mathbf{z}_i^{(\text{stat})}\right) + \varepsilon_i. \end{aligned} \quad (2)$$

## 2.2. Limitations and applicability

The synthetic data generation simulates acceleration time-histories, displacement data, and assumes temperature measurements. The datasets obtained consist of an artificial dataset with heterogeneous data, similar to the one that would be obtained by an environmental, static, and dynamic monitoring system. However, assumptions made about static load applications and damage conditions limit the comprehensiveness of the datasets. Currently, the benchmark does not account for non-linearities related to material properties, geometry, constraints, or dependencies on operational and environmental conditions other than the one described before. Some simplifications were adopted intentionally, starting with the linear material behaviour; the disregard for the stiffness contribution of the slab in bending; the simulation of the temperature affected steel stiffness only through an empirical relationship, leaving aside other environmental drivers and possible coupled effects due to differences in exposure and thermal response due to geometric specificities. Uncertainty was treated probabilistically only for

the live-load process; uncertainties in geometry, material properties, and constraints were not propagated. These were conscious trade-off to generate informative labelled data in a reproducible way. The modelling of the ambient excitation did not include more advanced effects such as the simulation of human walking on top of the slab, the wind effect or the effects of micro-tremors and seismic activity. Although the dataset achieves a high level of realism, several extensions could have been implemented to include further complexity and introduce richer uncertainties like the following: the addition of nonlinearity such as contact/slip at supports; the use of stochastic processes as ambient excitation, calibrating them on real measured indoor/outdoor activity, wind, micro-tremors, and nearby traffic; the refinement of the relationship with EVs to include thermal gradients, expansion effects on geometry, and mass-dependent stiffness under high occupancy; the addition to maintenance events to the SF/M simulations, and finally the expansion of the structure setup to a multiple DOFs model and the simulations of an array of accelerometers, enabling the use of mode shapes and modal flexibility matrix as DSFs. However, the open-source code offers opportunities for future expansions. Overall, this dataset serves as a comprehensive, publicly accessible benchmark to advance SHM research and testing damage detection algorithms, with applications in academic and practical settings.

### 3. Benchmark design

#### 3.1. Geometry, materials and constraints

The chosen benchmark structure for simulated monitoring data generation is a steel beam IPE400 supporting a concrete slab that does not contribute to the stiffness of the section. The beam was assumed to belong to a structure located in Florence destined for residential use, and to be fixed at each end. Left-end and right-end supports of the beam are indicated as A and B, respectively. Geometric dimensions, material parameters, boundary constraints, and loading conditions were defined to balance realism with computational efficiency. The characteristics of the structure used as an initial reference are shown in Table 2, in terms of geometry, materials, loads, and boundary conditions.

#### 3.2. Operational conditions

Changes in the static live load were introduced to simulate fluctuations in the dynamic behaviour induced by variability in normal use as well as exceptional crowding events, and were reflected through variations in the structural mass. The permanent load  $p_G$ , due to self-weight, was deterministically calculated and kept constant throughout the monitoring period. Conversely, the live load  $p_Q$  was not treated as time-invariant (as reported in Table 3), but was modelled probabilistically according to the Probability Model Code of the Joint Committee on Structural Safety (JCSS) [12]. Two components of the live load were generated: a sustained (long-term) component  $p_{Q,lt}(t)$  and an intermittent (short-term) component  $p_{Q,st}(t)$ , accounting for occupancy variability and possible crowded events. The total load acting on the structure was defined according to a serviceability limit state (SLS) combination [13], as per Eq.3).

$$p_{des}(t) = 1.0 p_G + 1.0(p_{Q,lt}(t) + p_{Q,st}(t)). \quad (3)$$

The sustained load  $p_{Q,lt}(t)$  was considered as a Poisson square wave stationary process, and its intensity, sampled from a Gamma distribution  $i_{lt,k} \sim \text{Gamma}(\alpha, \beta)$ , remains constant between occupancy changes. The parameters  $\alpha$  and  $\beta$ , shape and rate of the Gamma distribution, respectively, were calculated from the mean and variance as  $m_{lt} = \frac{\alpha}{\beta}, \sigma_{lt}^2 = \frac{\alpha}{\beta^2}$ . Mean  $m_{lt}$  and variance  $\sigma_{lt}^2$  were chosen with reference to the equations (2.2) and (2.3) in [8] with parameters from Table 2.2.1 also in [12] (see Eq.4 and Table3). The variance was defined as per Eq.4:

$$\sigma_{lt} = \sqrt{\sigma_v^2 + \sigma_u^2 \kappa \frac{A_0}{A}}, \quad (4)$$

**Table 2.** Geometry, material properties and constraints

Description	Symbol	Quantity	Units [ ]
<b>Geometry</b>			
Length from A to B	$L$	6000	mm
Beam tributary area	$A_s$	$30 \cdot 10^6$	mm <sup>2</sup>
Thickness of the concrete slab	$t_s$	180	mm
Cross-section IPE400	$A$	$84.46 \cdot 10^4$	mm <sup>2</sup>
Section height	$h$	400	mm
Flange width	$b$	180	mm
Web thickness	$t_w$	8.60	mm
Flange thickness	$t_f$	13.50	mm
Inertia moment around strong axis	$I_{xx}$	$231.30 \cdot 10^6$	mm <sup>4</sup>
Elastic section modulus	$W_{el}$	$1156 \cdot 10^3$	mm <sup>3</sup>
Plastic section modulus	$W_{pl}$	$1307 \cdot 10^3$	mm <sup>3</sup>
<b>Materials</b>			
Young's modulus steel	$E_0$	210000	MPa
Yield strength steel S235	$\sigma_y$	235	MPa
Steel partial safety coefficient	$\gamma_s$	1.05	[ ]
Yield design strength steel S235	$f_{yd}$	$\sigma_y/\gamma_s = 223.9$	MPa
Density of steel	$d_s$	7850	kg/m <sup>3</sup>
Density of reinforced concrete	$d_c$	2500	kg/m <sup>3</sup>
<b>Constraints</b>			
Horizontal displacement constrained	$x_A, x_B$	0	m
Vertical displacement constrained	$y_A, y_B$	0	m
Rotation at the supports constrained	$\phi_A, \phi_B$	0	rad
<b>Reference time-invariant loads</b>			
Self-weight beam	$p_b$	0.65	kN/m
Self-weight slab	$p_s$	22.07	kN/m
Non-structural dead loads	$p_{G2}$	6.0	kN/m
Total structural dead load	$p_{G1}$	$= p_b + p_s = 22.72$	kN/m
Total dead load	$p_G$	$= p_{G1} + p_{G2} = 28.72$	kN/m
Reference time-invariant live load	$p_Q$	15.0	kN/m

where  $\kappa$  represents the influence-line shape factor (assumed equal to 1), and  $A_0/A$  is the ratio between the reference area and the tributary area  $A$  (with  $A > A_0 = 20 \text{ m}^2$ ).

The time intervals between the sustained load changes were calculated by sampling them from an exponential distribution. Mean and variance of the exponential distribution ( $m = \frac{1}{\lambda}$  and  $\sigma^2 = \frac{1}{\lambda^2}$ ) used for the rate of change, were calculated from the renewal rate  $\lambda$  also provided in Table 2.2 in [12].

The intermitted load  $p_{Q,st}(t)$  was instead modelled as a Poisson spike non-stationary process, with intensity also assumed to have a Gamma distribution (with mean  $m_{st}$  reported in Table 3 and variance  $\sigma_{st}$  from Eq.5 and an exponential distribution for the definition of the time of occurrence.

$$\sigma_{st} = \sqrt{\sigma_u^2 \kappa \frac{A_0}{A}}. \quad (5)$$

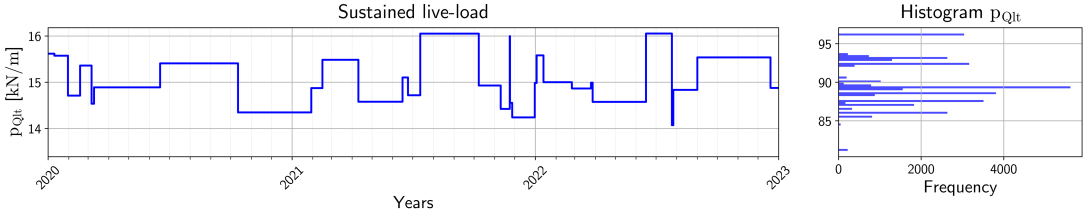


**Figure 4.** Simulated variability of the applied live load in time.

The scale of the exponential distribution used for the intermitted load was defined as the inverse of the number of occurrences per year ( $\nu$ ). Each intermitted load event duration was considered constant and set to 5 days. The generated load profile is plotted in Fig.4. Finally, in order to verify the designed beam considering both an ultimate limit state (ULS) and a serviceability limit state for irreversible effects (SLS) [13] were taken into account (see Table 3).

The two live load components are combined over the simulation period to represent the total live load [14, 15]. Note that the selected rate of occurrence of the intermitted load is significantly higher than the value recommended in [8], and the mean and rate of change of the sustained load have also been adjusted (strike-through and highlight in Table 4). These adjustments were made in order to better align with the data generation objective, which is to simulate a realistic operational variability range keeping the ratio between permanent/live load within the calculated reference, while the JCSS guidelines aim at reliability analysis at limit states exceedance.

**Table 3.** Parameter for live loads for used category residential. Some parameters were adjusted with respect to those recommended in [12], reported in brackets

Description	Symbol	Quantity	Units [ ]
Reference minimum influence area	$A_0$	20	$\text{m}^2$
Mean load intensity (lt)	$m_{lt}$	3(0.3)	$\text{kN}/\text{m}^2$
Global load intensity std parameter (lt)	$\sigma_v$	0.15	$\text{kN}/\text{m}^2$
Local load intensity std parameter (lt)	$\sigma_u$	0.3	$\text{kN}/\text{m}^2$
Sustained load intensity std parameter	$\sigma_{lt}$	0.07	$\text{kN}/\text{m}^2$
Inverse of the renewal rate	$1/\lambda$	10(7)	year
Mean load intensity (st)	$m_{st}$	0.3	$\text{kN}/\text{m}^2$
Load intensity std parameter (st)	$\sigma_U$	0.4	$\text{kN}/\text{m}^2$
Standard deviation of the load intensity (st)	$\sigma_{st}$	0.03	$\text{kN}/\text{m}^2$
Inverse of occurrences per year	$1/\nu$	0.2(1)	year
Inter-arrival duration intensity	$d_p$	5	days

### 3.3. Environmental conditions

The Young's Modulus  $E$  of steel was varied in each simulation as per Eq.6), in which  $E_0$  is the reference value of  $E$  at  $20^\circ\text{C}$ ,  $T^*$  the surface temperature,  $\alpha_T$  an amplification parameter added to scale the temperature effect. The constants  $e_1$ ,  $e_2$ ,  $e_3$ , and  $e_4$  were experimentally obtained in [16].

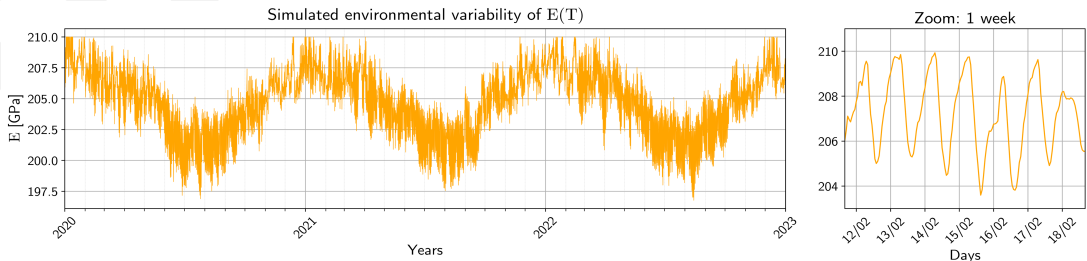
$$E(T) = E_0 \left( 1 - \alpha_T \cdot T^* \right) \exp \left[ -\frac{1}{2} \left( \frac{T^*}{e_3} \right)^{e_1} - \frac{1}{2} \left( \frac{T^*}{e_4} \right)^{e_2} \right] \quad (6)$$

The time-series of temperature was obtained from the recording of a sensor in the vicinity of the Structure and material testing Lab of the University of Florence. To accentuate the effect of temperature,

**Table 4.** Extreme values for live loads for the selected profile and serviceability limit checks

Description	Symbol	Quantity	Units [ ]
Maximum sustained live load	$p_{Qlt,max}$	16.05	kN/m
Minimum sustained live load	$p_{Qlt,min}$	13.51	kN/m
Maximum intermitted live load	$p_{Qst,max}$	4.18	kN/m
Minimum intermitted live load	$p_{Qst,min}$	0.00	kN/m
Maximum live load	$p_{Q,max}$	$\max(p_Q(t)) = 19.11$	kN/m
Minimum live load	$p_{Q,min}$	$\min(p_Q(t)) = 11.51$	kN/m
Average live load	$p_{Q,avg}$	$\text{avg}(p_Q(t)) = 15.01$	kN/m
Maximum ratio with permanent load	$\frac{p_{Q,max}}{p_G}$	67.29	%
Minimum ratio with permanent load	$\frac{p_{Q,min}}{p_G}$	47.83	%
Maximum total load ULS	$p_{des,ULS,max}$	67.20	kN/m
Maximum acting moment ULS	$M_{A,ULS}$	201.60	kN m
Maximum deflection due to $p_Q$	$\delta_{des,Q,max}$	1.32	mm
Average design load ULS	$p_{des,ULS}$	61.04	kN/m
Average design load SLS	$p_{des,SLS}$	43.72	kN/m
Resisting moment	$M_R$	$W_{el} \cdot f_{yd} = 258.84$	kN m
Acting moment ULS	$M_{A,ULS}$	$\frac{p_{des,ULS} L^2}{12} = 183.12$	kN m
Deflection limit for $p_G$	$\delta_{lim,G}$	$\frac{L}{250} = 24$	mm
Deflection limit for $p_Q$	$\delta_{lim,Q}$	$\frac{L}{300} = 20$	mm
Maximum deflection due to $p_G$	$\delta_{des,G}$	$\frac{p_G L^4}{384 E I_x} = 1.99$	mm
Maximum deflection due to $p_Q$	$\delta_{des,Q}$	$\frac{p_Q L^4}{384 E I_x} = 1.04$	mm

an amplification parameter ( $\alpha_T = 0.0015$  in Eq.6) was included to increase the effect of environmental variability on Young's modulus (see Fig.5). This amplification was applied to obtain a variability in natural frequency consistent with values found in the literature and observed in real case studies.

**Figure 5.** Simulated variability of the steel Young's Modulus with temperature.

### 3.4. Dynamic and static response

For dynamic response simulation, specific frequency bands were targeted by two band-pass filters to simulate the effects of human activities and vehicular traffic. To differentiate the two actions, two Gaussian inputs were generated for each hour of monitoring (acquisition), their standard deviation was randomly sampled within specific ranges (see Table 5), filtered and then superimposed to get the  $\omega_{AV}$  input. An example is provided in Fig. 6).

**Table 5.** Ambient vibration simulation

Description	Symbol	Quantity	Units
Sampling frequency	$f_s$	100	Hz
Signal length	$l_s$	180	s
Time interval	$dt$	0.01	s
Frequency resolution	$\Delta f$	0.0056	Hz
Human interaction	$f_{range}$	1.2 – 4.8	Hz
	$\sigma_{range}$	$5 \times 10^{-6}$ – $5 \times 10^{-4}$	$m/s^2$
Traffic	$f_{range}$	7 – 15	Hz
	$\sigma_{range}$	$1 \times 10^{-6}$ – $2 \times 10^{-4}$	$m/s^2$

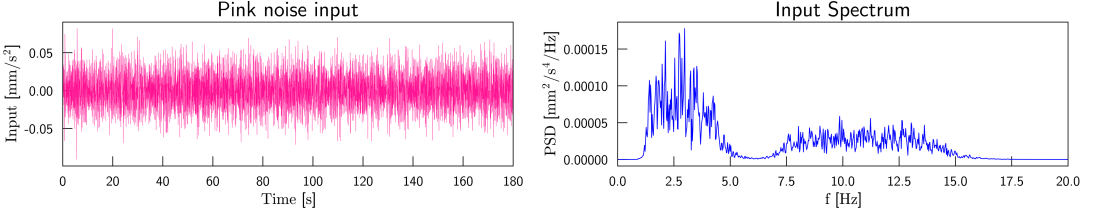


**Figure 6.** Example of coloured input for ambient vibration simulation.

A state-space approach was used to solve the equation of motion to calculate the dynamic structural response of the SDOF system, given the calculated equivalent stiffness dependent on  $E$  and therefore dependent on the temperature,  $k(T(t))$ , the equivalent mass calculated from the time-varying imposed static load,  $m(l(t))$ , the damping coefficient  $c$  ( $c = 2\zeta m\sqrt{k/m}$  with  $\zeta = 5\%$ ), and the defined input vibration  $\omega_{AV}$ . The method allows the addition of measurement noise  $\omega_M$ , even if in the current data generation it was not introduced. The state variables, displacement  $x_1 = x(t)$  and acceleration  $x_2 = \dot{x}(t)$ , were substituted into the equation of motion, leading to a system of two first-order differential equations (see Eq. 7).

$$\dot{\mathbf{x}}(t) = \begin{bmatrix} 0 & 1 \\ -\frac{k}{m} & -\frac{c}{m} \end{bmatrix} \begin{bmatrix} x_1 \\ x_2 \end{bmatrix} + \begin{bmatrix} 0 \\ \frac{1}{m} \end{bmatrix} (\omega_{AV} m) + \begin{bmatrix} 0 \\ \frac{1}{m} \end{bmatrix} \omega_M \quad (7)$$

It was verified that the maximum weighted acceleration generated by the simulation was within the limits for human comfort for both day and night vibrations, according to UNI 9614–2017 [17] and ISO 2631–2014 [18].

For the static response simulation, the single value of the deflection at mid-span for the reference fixed-fixed Euler-Bernoulli beam under the time-varying uniformly distributed load was calculated for

the static monitoring simulation. The formula used for the serviceability limit checks was also used for the generation of the static response (see Table 4). The deflection results for the undamaged condition simulated for the 3 years of monitoring are shown in Fig. 7.

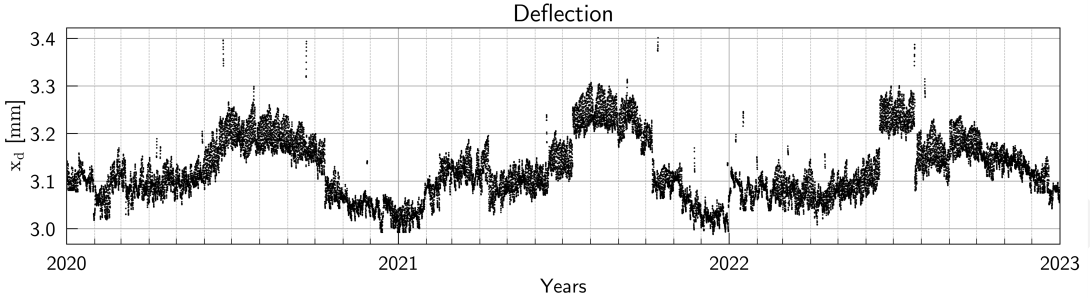


**Figure 7.** Simulated static monitoring: mid-span deflection with the effect of EOVs.

### 3.5. Damage simulation

Damage can be considered as a phenomenon which leads to a variation or a deviation from the initial or undamaged configuration, affecting the properties of the structural system ( $k_i, m_i$  in the present case). Referring to the equivalent stiffness formulation reported in Figure 2, damage was modelled as a localized stiffness reduction representing a condition such as the loosening of a connection, or partial yielding at a specific section of the beam. It was considered affecting only  $I$  with a decay rate of  $r = \Delta I / I_{UD}$ , yielding a stiffness variation from the undamaged (UD) condition equal to  $\Delta k = k_{UD} r$ . Since the natural frequency depends on stiffness as  $f \propto \sqrt{k}$ , the corresponding frequency variation followed as  $\frac{\Delta f}{f_{UD}} = \sqrt{r}$ . To contextualize the imposed stiffness reductions within the mechanical capacity of the reference section, plastic limit states were evaluated by comparing the elastic resisting moment  $M_{R,el}$  with the maximum acting bending moment  $\max(M_A(t))$ , defining a critical decay rate (Eq. 8).

$$r_{pl} = \frac{M_{R,el} - \max(M_A(t))}{M_{R,el}}. \quad (8)$$

Leading to the corresponding stiffness and frequency limits  $\Delta k_{pl} = k_{UD} r_{pl}$  and  $\Delta f_{pl} = f_{UD} \sqrt{r_{pl}}$ . Similarly, serviceability limits under permanent and live loads were derived assuming the deflection scaled inversely with stiffness ( $\delta \propto 1/k$ ). For each deflection limit  $\delta_{lim}$ , the associated decay rate is as per Eq. 9.

$$r_{lim} = 1 - \frac{\delta_{des}}{\delta_{lim}}, \quad (9)$$

From Eq. 9 the corresponding stiffness and frequency variations follow directly as  $\Delta k_{lim} / k_{UD} = r_{lim}$  and  $\Delta f_{lim} / f_{UD} = \sqrt{r_{lim}}$ . These limits are computed and summarized in Figure 8. The plastic stiffness decay was found to be  $\Delta k_{pl} = 29.3\%$ , while the serviceability limits in terms of stiffness and frequency variations were well beyond the plastic threshold.

#### 3.5.1. Fast-varying damage

Considering the modelling approach described, three configurations of sudden, FAST damage were simulated, as shown in Table 8 in Section 5 describing the generated data. A 1% reduction in  $k_i$  corresponded approximately to a 0.5% decrease in the analytical natural frequency  $f_n$  and to a 1% change in the midspan resisting moment  $M_R$ , assuming stiffness loss modelled as inertia reduction. With reference to Figure 8, the listed percentage reductions of stiffness were chosen restricting the variability of interest to the elastic range. Since EOVs were found to induce frequency variations of up to about 4% and 6%,

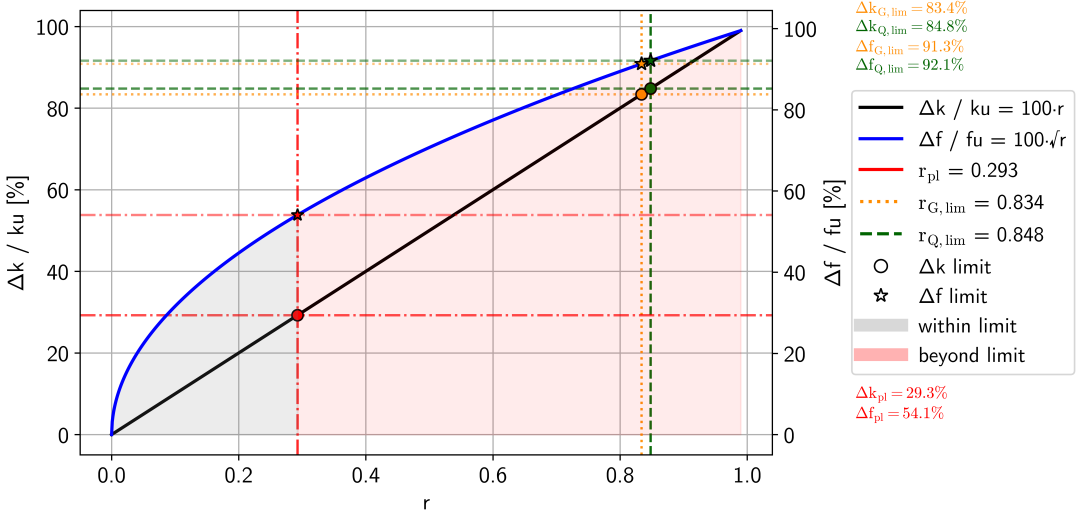


**Figure 8.** Variation of stiffness ( $\Delta k/k_{UD}$ ) and frequency ( $\Delta f/f_{UD}$ ) as a function of the rate of decay of the stiffness  $r$ .

respectively, and FAST-induced stiffness drops was simulated to cumulate with these effects, they were generally kept below 28%, with only a limited portion of one dataset reaching  $\Delta k = 32\% > \Delta k_{pl}$ . This choice was made to allow the evaluation of the detectability of damage as it approaches, and eventually exceeds, the plastic threshold.

### 3.5.2. Slow-varying damage

Damage was also modelled as diffused and slow-varying, representing corrosion as a progressive and uniform thickness reduction of the cross-section at a prescribed rate. This gradual section loss meant a decrease in inertia and, consequently, stiffness, as well as a smaller reduction in mass due to volume loss. SLOW damage therefore translates into a progressive reduction of the equivalent stiffness  $k_i$  and, to a lesser extent, of the mass  $m_i$  across acquisitions, reflecting the gradual deterioration of structural properties over time.

Among the mechanisms leading to slow-varying damage, corrosion was selected as the most representative for metallic components. Its evolution is non-linear: corrosion progresses rapidly at early stages due to direct exposure to environmental agents, then slows as a protective oxide layer forms and partially shields the surface. Over longer periods, the extent of corrosion depends on the penetration of water and reactive substances through defects in this layer. To account for environmental influence, a relationship proposed in 2007 [19] was adopted, as it explicitly models the interaction between corrosion and environmental variables (see Eq. 10).

$$d(t) = A \cdot t^B \cdot \left(\frac{\text{TOW}}{C}\right)^D \cdot \left(1 + \frac{[\text{SO}_2]}{E}\right)^F \cdot \left(1 + \frac{[\text{Cl}]}{G}\right)^H \cdot e^{J(T+T_0)} \quad (10)$$

The rate of corrosion is expressed in Eq. 10., in which:

- $d$  is the corrosion loss expressed in [ $\mu\text{m}$ ] as a function of  $t$ , the exposure time [years], considering here the exposure to start after 1.5 years from the beginning of monitoring;
- TOW is the annual time of wetness [h/year], the fraction of time that the metal surface remains wet. For simplicity, the TOW was approximated as the overall time in which the RH is greater than 80% and the temperature is greater than 0°C [20] within one year;
- $\text{SO}_2$  and Cl are respectively the sulphur dioxide concentration and the chloride deposition rate for non-marine environments;

- $T_{avg}$  is the average temperature in [°C] within one year;
- $A, B, D, E, F, G, H, J$  and  $T_0$  are coefficients proposed in [19] adapted for the present case.

The corrosivity category adopted was “ISO9223 C3 Medium: Temperate zone with medium pollution” ( $5 < SO_2, [\mu g/m^3] < 30$ ) with low chloride effect, representative of urban or mildly coastal environments. Although the selected model may overestimate long-term corrosion, it provided a relationship explicitly linked to environmental parameters. Using the average environmental values for 2020, the corrosion rate was estimated as  $47.03 \mu m/year$  ( $0.04703 mm/year$ ), corresponding to approximately  $0.2 mm$  over the 3-year monitoring period and to a 35% flange thickness loss over a hypothetical 100-year exposure. Three corrosion scenarios were analysed: the estimated rate and accelerated rates of  $10\times$  and  $20\times$ , including their effects on mass and stiffness. The resisting moment at the end of the monitoring period was also evaluated: the structure remains in the elastic range for the first level, reaches the plastic range for the second, and does not satisfy the safety check for the third.

### 3.6. Sensor faults and malfunctions simulation

Sensor faults or malfunctions were simulated by introducing typical anomalous patterns into the acceleration signals. Similar patterns could be used to contaminate also the displacement measurements across the whole time series, with the exception of a few faults or malfunctions that are specific to accelerometers (e.g. cable detachment). Most expected faults/malfunctions were identified, based on literature research [21–23] and on the authors’ experience with real monitoring data (see Figure 9). An illustration of all simulated sensor faults and malfunctions is displayed in Figures 10 and 10, distinguishing seven categories of sensor faults/malfunctions (Table 6):

1. Drifting (D): gradual change in the sensor’s output over time;
2. Bias or Shift (B): consistent offset in the sensor output, they can occur also as a result of drift in previous acquisitions;
3. Spikes (S): large amplitude value at a specific instant;
4. Gain (G): amplification or attenuation of the signal;
5. Noise (N): overlaid Gaussian noise onto the signal;
6. Missing Data (M): Gaps within the time series;
7. Cable Detachment (C): sinusoidal wave that rapidly decreases in amplitude, simulating a sensor that disconnects either momentarily or completely.

**Table 6.** Typologies of sensor faults simulated

Class	Formulation		Ranges of variability
D	$a_D(\tau) = a(\tau) + s_D \cdot \exp\left(-\frac{\tau}{l_s/10}\right) + s_D$	$\tau \in [\tau_{st}, \tau_{end}]$	$s_D = 1e^{-3} \div 2e^{-3} [m/s^2]$
B	$a_B(\tau) = a(\tau) + s_B$	$\tau \in [\tau_{st}, \tau_{end}]$	$s_B = 1.2 \div 1.7 [m/s^2]$
S	$a_S(\tau) = a(\tau) + s_S \cdot (\Delta\tau_S)$	$\tau \in [\tau_{st}, \tau_{end}]$	$s_S = 5e^{-2} \div 5e^{-3} [m/s^2]$ $\Delta\tau_S = 0.1 \cdot f_s \div 0.2 \cdot f_s [-]$
G	$a_G(\tau) = a(\tau) \cdot s_G$	$\tau \in [\tau_{st}, \tau_{end}]$	$s_G = 1.1 \div 3.1 [m/s^2]$
N	$a_N(\tau) = a(\tau) + \eta(\tau)$	$\tau \in [\tau_{st}, \tau_{end}]$	$s_N = 1e^{-3} \div 1e^{-5} [m/s^2]$
M	$a_M(\tau) = \text{null or missing}$	$\tau \in [\tau_{st}, \tau_{end}]$	$\tau_{st} = 0.8 \div 0.2 \Delta t [-]$ $f_C = 0.5 \div 1.5 [Hz]$
CD	$a_C(\tau) = s_C \sin(2\pi f_C \tau) \exp(-\lambda_C \tau)$	$\tau \in [\tau_{st}, \Delta\tau_C]$	$s_C = 0.05 \div 0.2 [m/s^2]$ $\lambda_C = 0.02 \div 0.05 [1/s]$

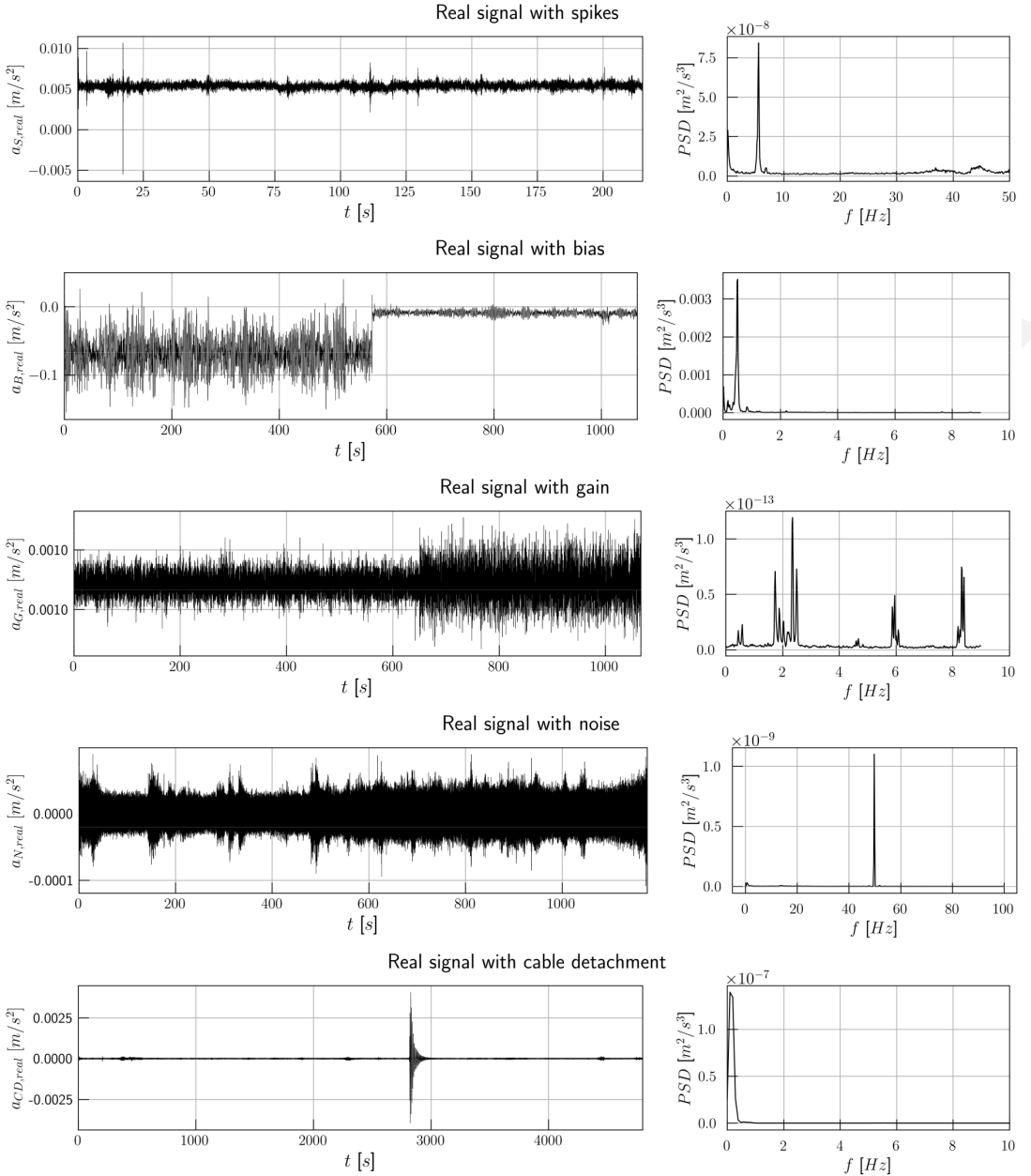


**Figure 9.** Samples for real data acquisitions for the simulated sensor faults and/or malfunctions.

Some of the chosen SF/M categories may apply to any vibration sensor, regardless of its type, while others are specific to certain typologies of sensors (e.g. cable detachment does not apply to wireless sensors). The categories were chosen based on their recurrence in the real data observed, but also to obtain a set of classes impacting damage sensitive features differently, as they show different effects in the frequency and time domain.

For each type, the mathematical formula for the simulation is provided in Table 6. In the formulas,  $a(\tau)$  denotes the original signal, while  $a_*(\tau)$  indicates the modified signal post-fault application, with

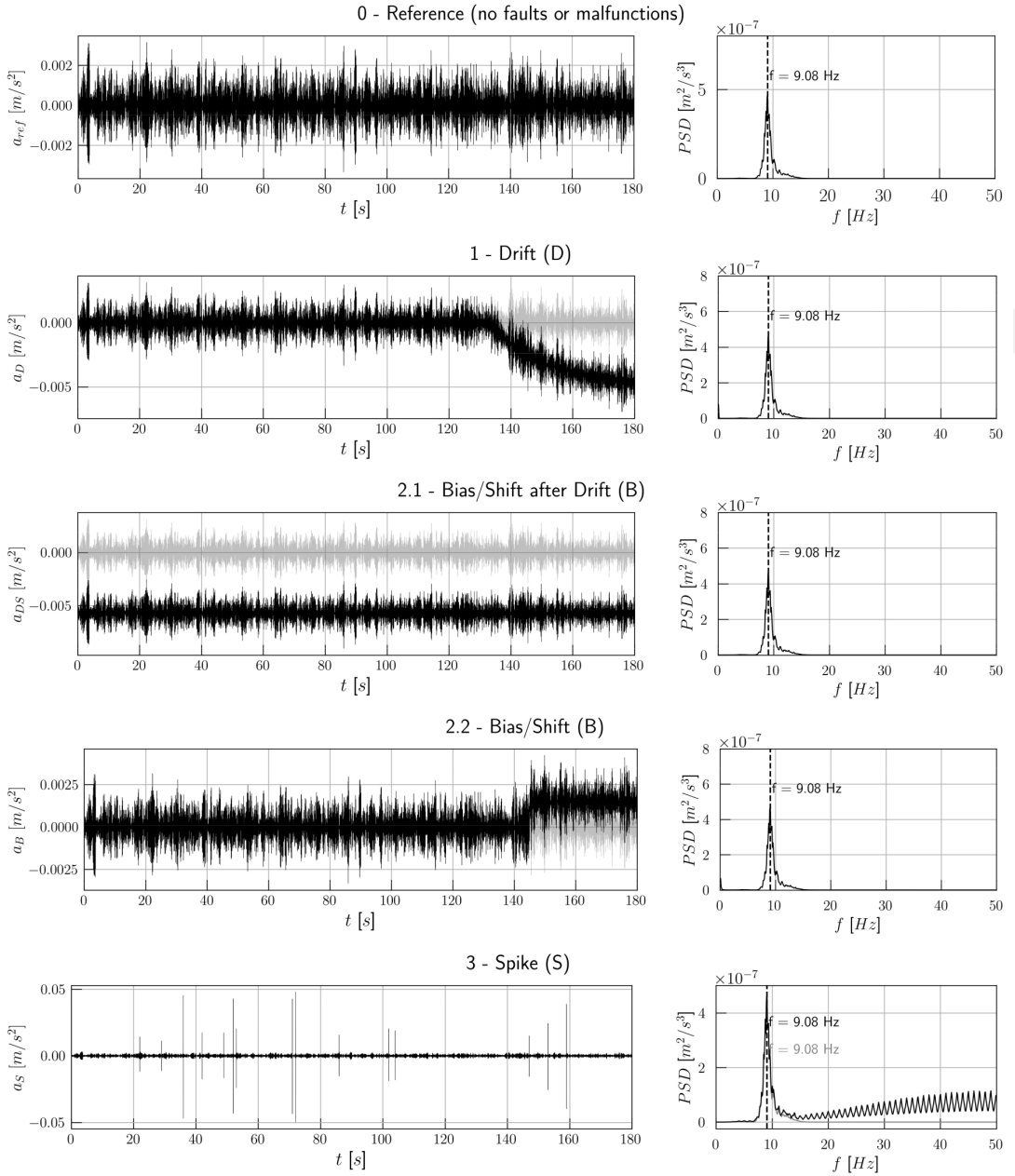


**Figure 10.** Example of generated SF/M in order from top to bottom: (0) reference acceleration signal, no faults or malfunctions (1) drift, (2) bias, (3) spikes. Each image shows the output in the time domain and the frequency domain.

variations dependent on the time progression  $\tau$  within each simulated acceleration acquisition, different from the time progression within the monitoring period  $t$  mentioned beforehand. The scale factor  $s_*$  quantifies the extent of each malfunction, calibrated according to the magnitude of measured accelerations.  $L_s$  represents the length of the signal,  $t_{st}$  marks the starting point for fault or malfunction application, randomly chosen, and  $t_{end}$  signifies the end of the signal time history. Specific durations for

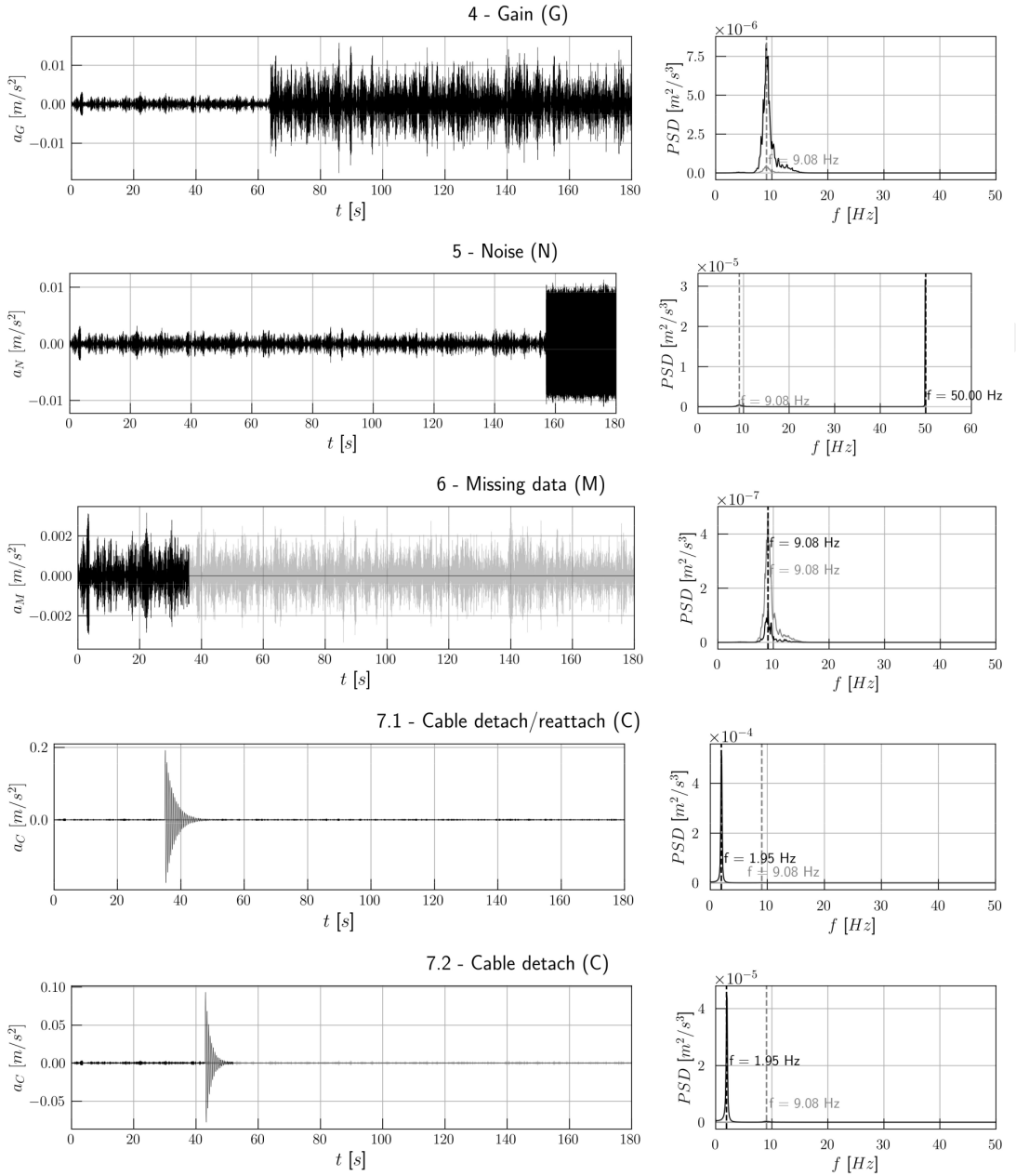


**Figure 11.** Example of generated SF/M in order from top to bottom: (4) gain, (5) noise, (6) missing data, and temporary (7.1) or permanent (7.2) cable detachment. Each image shows the output in the time domain and the frequency domain.

spikes and cable detachment are denoted by  $\Delta t_*$ . Gaussian noise  $\eta(\tau)$  is characterized by a zero mean and a standard deviation  $s_N$  that mirrors the sensor noise level. In cable detachment simulations,  $s_C$  defines the initial amplitude of the sinusoidal wave,  $f_C$  its frequency, and  $\lambda_C$  its decay rate, which leads to a rapid amplitude decrease following detachment onset. Spikes were simulated as single acquisition

faults, as well as instances of cable detachment and immediate reattachment. All the other faults were simulated as prolonged effects over a randomly selected range of acquisition between 5 and 25.

#### 4. Data generation

Leveraging the capabilities of parallel computing, the benchmark utilized the processing power of an Intel Core i7-8750H processor with 12 cores at 2.2 GHz to simulate the three years of monitoring data in 2.5 hours, utilizing Python 3.11 and the Ray package for implementation. A comprehensive summary of the data generation process with parallel computing is detailed in algorithm 1. All typologies of the generated sub-dataset are listed in Table 7. Minimal fluctuations of the generated input spectrum could cause variabilities in the output spectrum and influence the subsequent feature extraction process such as natural frequency identification. In order to attenuate this effect and keep the inherent error within realistic limits, each dynamic simulation was repeated up to ten times, with a tolerance threshold established at 1% of the reference frequency for the simulations. This value is consistent with realistic fluctuations of the extracted frequencies. If the simulations did not achieve a frequency within this margin, the generated signal providing the closest frequency value among the ten iterations was selected. The algorithm used for data generation is elaborated in Table 6 below.

---

#### Algorithm 1 Dynamic Data Generation with Parallel State-Space Simulations

---

```

1: Load  $n_{\text{CPUs}}$  samples from matrix  $M \in \mathbb{R}^{n_a \times 2}$ 
2: Generate time series with hourly intervals and filter leap years
3: Setup methods for input generation, state-space simulation, frequency check
4: Initialize parallel computation on  $n_{\text{CPUs}}$ 
5: for each core  $c = (1, \dots, n_{\text{CPUs}})$  do
6:   Select one sample  $(k_i, m_i)$ 
7:   while  $n_{\text{sim}} < n_{\text{sim,max}} = 10$  do
8:     Generate input signal with length  $n_s$ 
9:     Apply passband filter (human interaction, traffic)
10:    Solve state-space equations for  $(k_i, m_i)$ 
11:    Compute Welch PSD
12:    Extract dominant frequency (peak PSD)
13:    if  $\frac{f_{n,\text{extr}}}{f_{n,\text{anal}}} < 1\%$  then
14:      Select acceleration and break
15:    else
16:      Increment  $n_{\text{sim}}$ 
17:    end if
18:  end while
19:  Select acceleration corresponding to best frequency
20:  Write selected acceleration to HDF5 file
21: end for
22: End parallel computing

```

---

#### 5. Dataset description

The full generated dataset consists of 9 sub-datasets of both dynamic and static synthetic acquisitions (see Table 7 and Figure 12). All data and scripts are contained in a database at the provided link in the

data availability statement. The reference simulation time covers a period of three years (e.g., 2020–2022), for each sampled hour, a simulated acceleration response was generated in the form of three-minute acceleration records with 100 samples per second, together with a single displacement value. The acceleration signals are provided in HDF5 (.h5) format, expressed in  $\text{m/s}^2$ .

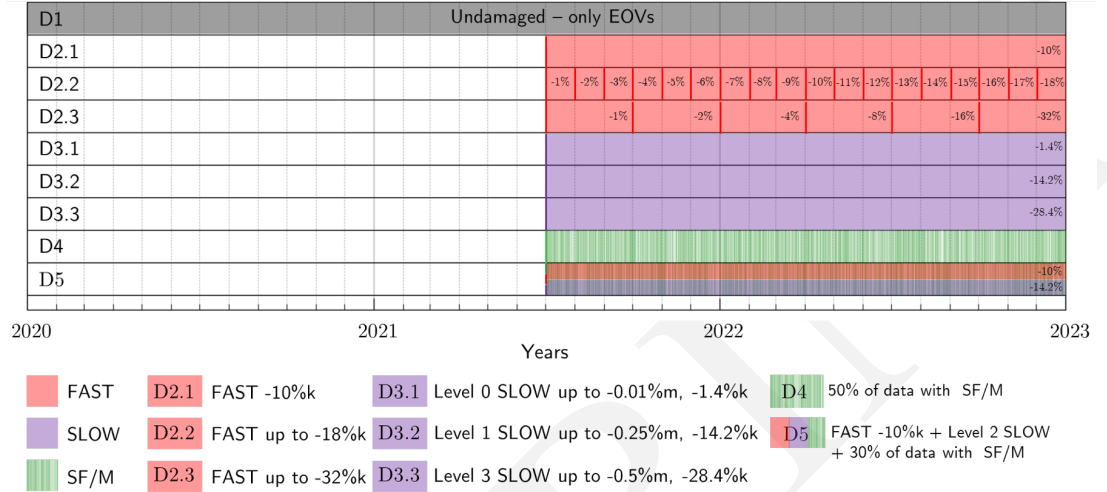


**Figure 12.** Qualitative representation of the sub-datasets content (in red FAST, in purple SLOW, in green SF/M).

Each acceleration file is named using the convention `accXXXXX-YZ.h5`, where XXXXX is a five-digit, zero-padded numerical code corresponding to the fixed 3-year time series,  $Y$  varies from 0 to 5 according to the sub-dataset to which the signal belongs, and  $Z$  corresponds to a subset alternative when present. Sub-datasets 2 and 3 both present three alternatives, simulating different levels of fast- and slow-varying damage; each alternative is indicated by adding an increasing number to the dataset index (i.e., `acc00000-21.h5` belongs to sub-dataset 2, alternative 1). To import each .h5 file, the denomination `acc` must be used.

Deflection acquisitions, expressed in mm, are provided in a single text file (`deflection_D1-5.txt`), arranged as a matrix, each column corresponding to sub-dataset  $Y$ . Each column of the matrix represents a sub-dataset (in this case the data generated for the reference initial period is repeated for each sub-dataset). Deflection data does not vary in sub-dataset 4, as it is not considered affected by sensor faults or malfunctions.

The first sub-dataset includes the complete time series with only the effect of EOVs on the undamaged structure. Each subsequent sub-dataset is generated as a portion of the initial undamaged dataset to include one or more of the following effects:

- The effect of fast-varying damage (FAST) acting suddenly on the data (shift), modelled as one or more sudden stiffness's ( $k$ ) decays.
- The effect of slow-varying damage (SLOW) acting progressively on the data (trend), simulating accelerated corrosion conditions at different rates, decreasing the area of the beam and therefore its stiffness ( $k$ ) and mass ( $m$ ).
- The effect of sensor faults and/or malfunctions (SF/M) applied *a posteriori* to the simulated acceleration data.

The time-varying loading and temperature profiles used are provided, together with the series of  $k$ - $m$  pairs used to generate each sub-dataset (all in .txt format in the folder input). Finally, 9 .txt files

**Table 7.** Generated datasets

Code	Description	Simulated effects	Duration	Num. Acq.	Dim. [GB]
D1	Undamaged (UD)	EOVs	3 years (01/01/2020-31/12/2022)	26280	1.90
D2.1	Fast varying damage (FAST)	1 single step -10% (max 10%)	1.5 years from index 13104 (01/07/2021-31/12/2022)	13176	0.98
D2.2		18 steps of -1% up to -18% each month		13176	0.98
D2.3		6 steps of increasing intensity (from 1% up to 32%, with geometric progression doubling by 2)		13176	0.98
D3.1	Slow varying damage (SLOW)	Ageing damage (Lev. 0)	1.5 years from index 13104 (01/07/2021-31/12/2022)	13176	0.98
D3.2		Accelerated corrosion (Lev. 1)		13176	0.98
D3.3		Accelerated corrosion (Lev. 3)		13176	0.98
D4	Sensor Faults and/or Malfunctions (SF/M)	$\leq 50\%$ of contaminated data equally distributed among 8 classes of sensor faults or malfunctions	6600 acquisitions randomly sampled in the period from index 13104 to the end	6623	0.49
D5	Overlap	FVD of dataset 2.3 and SVD of dataset 3.3 overlapped with 30% of the data contaminated with sensor faults or malfunctions	1.5 years from index 13104 (01/07/2021-31/12/2022)	13176	0.98

containing labels for all datasets are provided (see Table 7). An example of an excerpt of the deflection dataset containing all deflection data is shown in Figure 13.

The code is provided in the form of four Jupyter Notebooks written for Python v. 3.11.9 containing the following information:

- Description of the definition of the EOVs applied (EOVs. ipynb).
- SDOF system modelling (SDOF. ipynb).
- Data generation script example (SHM. ipynb).
- Sensor faults/malfunctions formulation and dataset contamination (SFM. ipynb).

Each notebook is documented to guide users in modifying simulations to generate new data or adjust assumed parameters. The data is ready for use *as is* or can be tailored using the provided code to explore different simulation scenarios, for example, simulating damage shifts at different indices or extending the monitoring period. The entire database occupies approximately 10 GB, encompassing all files from

	D1	D21	D22	D23	D31	D32	D33	D5
26275	3.063	3.224	3.670	4.298	3.127	3.774	4.682	4.523
26276	3.068	3.229	3.676	4.306	3.132	3.781	4.690	4.531
26277	3.070	3.231	3.678	4.308	3.134	3.783	4.693	4.533
26278	3.068	3.229	3.676	4.305	3.132	3.781	4.690	4.530
26279	3.069	3.230	3.677	4.306	3.133	3.782	4.692	4.532

**Figure 13.** Excerpt of the tail of the deflection dataset; sample IDs in the first column, deflection values are in mm.

all sub-datasets for the three-year monitoring period. The database therefore includes the generated data, all all necessary input data for the generation, and the code required to operate the simulation.

## 6. Conclusions, limitations and applicability

This paper presented the design and development of a controlled, multi-year numerical SHM data benchmark including environmental and operational variabilities, fast and slow-varying damage mechanisms, and sensor faults/malfunctions within a single framework. The case study consisted of a fixed steel beam, modelled with Euler-Bernoulli theory for the static response and an equivalent SDOF representation for the dynamic response. Three years of hourly static deflection and three-minute ambient vibration acquisitions were simulated, with explicit variability of live load, ambient excitation content, temperature-dependent stiffness, sudden stiffness drops (FAST), progressive stiffness/mass loss (SLOW), and seven classes of sensor faults (drift, spikes, bias, gain, noise, missing data, cable detachment) applied a posteriori to the simulated accelerations. The dataset was organised into 9 sub-datasets to be used for specific purposes. Specific formulations were chosen to simulate EOVs and damage, while each SF/M type was formalised with parameters and variability ranges to yield reproducible contaminations that mirrored realistic effects observed in real data. Overall, the benchmark paired static and dynamic responses under a coherent set of evolving loads, temperatures, damages, and anomalies, enabling future testing on single effects and on their interactions. As open numerical datasets for SHM remain limited, particularly where environmental/operational variability, long-term damage, and sensor issues co-exist, and experimental campaigns are still too costly to scale, the objective of this dataset development was to address this gap with a computationally inexpensive benchmark that would yet retain the essential behaviours that drive many vibration-based DSFs, and that could be used directly to apply statistical, ML, and DL approaches for system identification, anomaly/damage detection, and robustness studies, including the current research. In the short term, the benchmark is currently serving as the test-bed for the development of further research on damage-sensitive features and damage identification [24]. In a longer-term perspective, leveraging the open code and datasets provided, the same benchmark design could be replicated, adjusted, and/or extended including more complex effects.

**Funding Statement.** The research was conducted during the course of a PhD International program at the University of Florence supported by a scholarship granted by Regione Toscana under the "Giovani" project, in cotutelle with the University of Minho and the Institute, with the additional support of the Erasmus + Traineeship Program.

**Competing Interests.** The authors declare that they have no known competing financial interests or personal relationships that could have appeared to influence the work reported in this paper.

**Data Availability Statement.** The dataset generated and the code used for its definition are publicly available through the Zenodo repository under the name SDOF SHM benchmark. The data can be accessed via the persistent identifier <https://doi.org/10.5281/zenodo.17900300>. The repository contains the full dataset required to reproduce the generate the data presented in this paper. The simulations were performed on servers at the University of Florence and the University of Minho.

**AI Use Statement.** The authors used an AI language model during the study preparation process to assist with text and code editing, proofreading and formatting. AI was not used to generate scientific results, analyses, or interpretations. All content was reviewed and validated by the author.

**Ethical Standards.** The research meets all ethical guidelines, including adherence to the legal requirements of the study country.

**Authors' Contributions.** Francesca Marafini: Conceptualization, Methodology, Software, Formal analysis, Investigation, Data Curation, Writing Original Draft, Writing Review and Editing, Visualization, Resources; Giacomo Zini: Conceptualization, Validation, Supervision, Writing - Review and Editing, Resources; Alberto Barontini: Conceptualization, Validation, Supervision, Writing - Review and Editing, Resources; Nuno Mendes: Supervision, Writing Review and Editing, Project Administration; Alice Cicirello: Conceptualization, Supervision, Writing Review and Editing; Michele Betti: Conceptualization, Supervision, Project Administration, Funding acquisition - Gianni Bartoli: Conceptualization, Supervision

## References

- [1] J. Maeck and G. De Roeck. Description of Z24 benchmark. *Mechanical Systems and Signal Processing*, 17(1):127–131, January 2003. ISSN 08883270. doi: 10.1006/mssp.2002.1548.
- [2] Marcus Haywood-Alexander, Robin S. Mills, Max D. Champneys, Matthew R. Jones, Matthew S. Bonney, David Wagg, and Timothy J. Rogers. Full-scale modal testing of a Hawk T1A aircraft for benchmarking vibration-based methods. *Journal of Sound and Vibration*, 576:118295, April 2024. ISSN 0022460X. doi: 10.1016/j.jsv.2024.118295.
- [3] K. Worden. Structural Fault Detection Using a Novelty Measure. *Journal of Sound and Vibration*, 201(1):85–101, March 1997. ISSN 0022460X. doi: 10.1006/jsvi.1996.0747.
- [4] Bjørn T. Svendsen, Gunnstein T. Frøseth, Ole Øiseth, and Anders Rønquist. A data-based structural health monitoring approach for damage detection in steel bridges using experimental data. *Journal of Civil Structural Health Monitoring*, 12(1):101–115, February 2022. ISSN 2190-5452, 2190-5479. doi: 10.1007/s13349-021-00530-8.
- [5] Konstantinos Tatsis and Eleni Chatzi. A numerical benchmark for system identification under operational and environmental variability. 2019. doi: 10.3929/ETHZ-B-000385231.
- [6] Konstantinos Tatsis, Yaowen Ou, Vasilis K. Dertimanis, Minas D. Spiridonakos, and Eleni N. Chatzi. Vibration-based monitoring of a small-scale wind turbine blade under varying climate and operational conditions. Part II: A numerical benchmark. *Structural Control and Health Monitoring*, 28(6), June 2021. ISSN 1545-2255, 1545-2263. doi: 10.1002/stc.2734.
- [7] B F Spencer, R E Christenson, and S J Dyke. Next Generation Benchmark Control Problem for Seismically Excited Buildings. 1999.
- [8] E. A. Johnson, H. F. Lam, L. S. Katafygiotis, and J. L. Beck. Phase I IASC-ASCE Structural Health Monitoring Benchmark Problem Using Simulated Data. *Journal of Engineering Mechanics*, 130(1):3–15, January 2004. ISSN 0733-9399, 1943-7889. doi: 10.1061/(ASCE)0733-9399(2004)130:1(3).
- [9] Jason Lee Burkett. *Benchmark Studies For Structural Health Monitoring Using Analytical And Experimental Models*. PhD thesis, University of Central Florida, Orlando, 2005.
- [10] Paolo Tiso and Jean-Philippe Noël. A new, challenging benchmark for nonlinear system identification. *Mechanical Systems and Signal Processing*, 84:185–193, February 2017. ISSN 08883270. doi: 10.1016/j.mssp.2016.08.008.
- [11] K Vlachas, K Tatsis, K Agathos, A R Brink, and E Chatzi. Two-story frame with Bouc-Wen hysteretic links as a multi-degree of freedom nonlinear response simulator.
- [12] JCSS Probabilistic Model Code Part 2: Load Models, May 2021.
- [13] Andrea Barocci. *Norme tecniche per le costruzioni 2018: le NTC 2018 (D.M. 17 gennaio 2018) e la loro applicazione: testo della norma, commento, confronto NTC 2008 e NTC 2018*. Maggioli, Santarcangelo di Romagna (RN), 2018. ISBN 978-88-916-1980-8.
- [14] Tom Vrouwenvelder, Milan Holicky, and Jana Markova. JCSS Probabilistic Model Code Part 4: Example applications, May 2021.
- [15] Luis G L Costa, Andre T Beck, and Wagner C Santiago. Stochastic live load model for buildings and its application in reliability-based code calibration. 2022.
- [16] Mina Seif, Joseph Main, Jonathan Weigand, Fahim Sadek, Lisa Choe, Chao Zhang, John Gross, William Luecke, and David McColskey. Temperature-Dependent Material Modeling for Structural Steels: Formulation and Application. Technical Report NIST TN 1907, National Institute of Standards and Technology, April 2016.
- [17] UNI 9614:2017 - Measurement of vibration in buildings and disturbance assessment criteria, September 2017.
- [18] UNI ISO 2631-1:2014 Mechanical vibration and shock - Assessment of human exposure to whole-body vibration - Part 1: General requirements. Adopting ISO 2631-1:1997., December 2014.
- [19] Dawn E. Klinesmith, Richard H. McCuen, and Pedro Albrecht. Effect of Environmental Conditions on Corrosion Rates. *Journal of Materials in Civil Engineering*, 19(2):121–129, February 2007. ISSN 0899-1561, 1943-5533. doi: 10.1061/(ASCE)0899-1561(2007)19:2(121).
- [20] Luigi Di Sarno, Armin Majidian, and George Karagiannakis. The Effect of Atmospheric Corrosion on Steel Structures: A State-of-the-Art and Case-Study. 11(12):571. ISSN 2075-5309. doi: 10.3390/buildings11120571. URL <https://www.mdpi>.

[com/2075-5309/11/12/571](https://doi.org/10.1007/s10071-023-01571-1).

- [21] Atia Javaid, Nadeem Javaid, Zahid Wadud, Tanzila Saba, Osama Sheta, Muhammad Saleem, and Mohammad Alzahrani. Machine Learning Algorithms and Fault Detection for Improved Belief Function Based Decision Fusion in Wireless Sensor Networks. *Sensors*, 19(6):1334, March 2019. ISSN 1424-8220. doi: 10.3390/s19061334.
- [22] Muhammad Ahmer, Fredrik Sandin, Pär Marklund, Martin Gustafsson, and Kim Berglund. Failure mode classification for condition-based maintenance in a bearing ring grinding machine. *The International Journal of Advanced Manufacturing Technology*, 122(3-4):1479–1495, September 2022. ISSN 0268-3768, 1433-3015. doi: 10.1007/s00170-022-09930-6.
- [23] Andreea-Maria Oncescu and Alice Cicirello. A Self-supervised Classification Algorithm for Sensor Fault Identification for Robust Structural Health Monitoring. In Piervincenzo Rizzo and Alberto Milazzo, editors, *European Workshop on Structural Health Monitoring*, volume 253, pages 564–574. Springer International Publishing, Cham, 2023. doi: 10.1007/978-3-031-07254-3\_57.
- [24] F. Marafini, G. Zini, A. Barontini, M. Betti, G. Bartoli, N. Mendes, and A. Cicirello. Long-Term Ageing Damage Identification in Vibration-Based Structural Health Monitoring. In Álvaro Cunha and Elsa Caetano, editors, *Experimental Vibration Analysis for Civil Engineering Structures*, pages 442–452. Springer Nature Switzerland. ISBN 978-3-031-96114-4. doi: 10.1007/978-3-031-96114-4\_46.